Monthly Notices
of the
ROYAL ASTRONOMICAL SOCIETY

MNRAS **480,** L12–L17 (2018)
Advance Access publication 2018 June 18

doi:10.1093/mnrasl/sly109

Observability of planet–disc interactions in CO kinematics

Sebastián Pérez,[1,2]★ S. Casassus[1,2]★ and P. Benítez-Llambay[3]

[1]*Departamento de Astronomía, Universidad de Chile, Casilla 36-D, Santiago, Chile*
[2]*Millennium Nucleus on 'Protoplanetary Disks', Casilla 36-D, Santiago, Chile*
[3]*Niels Bohr International Academy, Niels Bohr Institute, Blegdamsvej 17, DK-2100 Copenhagen Ø, Denmark*

Accepted 2018 June 11. Received 2018 June 08; in original form 2018 May 3

ABSTRACT

Empirical evidence of planets in gas-rich circumstellar discs is required to constrain giant planet formation theories. Here we study the kinematic patterns which arise from planet–disc interactions and their observability in CO rotational emission lines. We perform 3D hydrodynamical simulations of single giant planets and predict the emergent intensity field with radiative transfer. Pressure gradients at planet-carved gaps, spiral wakes, and vortices bear strong kinematic counterparts. The isovelocity contours in the CO(2-1) line centroids $v_\circ$ reveal large-scale perturbations, corresponding to abrupt transitions from below *sub*-Keplerian to *super*-Keplerian rotation along with radial and vertical flows. The increase in line optical depth at the edge of the gap also modulates $v_\circ$, but this is a mild effect compared to the dynamical imprint of the planet–disc interaction. The large-scale deviations from the Keplerian rotation thus allow the planets to be indirectly detected via the first moment maps of molecular gas tracers, at Atacama Large Millimetre/submillimetre Array angular resolutions. The strength of these deviations depends on the mass of the perturber. This initial study paves the way to eventually determine the mass of the planet by comparison with more detailed models.

Key words: hydrodynamics – methods: numerical – planets and satellites: detection – planet–disc interactions – protoplanetary discs.

1 INTRODUCTION

The detection of protoplanets via direct imaging has been notoriously difficult, requiring extreme high-contrast data and substantial image filtering. At this point, it is not clear whether the candidate detections correspond to point-like emission (Sallum et al. 2015) associated with a circumplanetary disc (CPD), residual disc features (Thalmann et al. 2016; Follette et al. 2017), or shock heating locally puffing up the edges of a gap (Hord et al. 2017). These technological barriers combined with large uncertainties in the initial conditions of evolutionary tracks (high- or low-entropy start models, Spiegel & Burrows 2012) hamper the unambiguous detection of protoplanets and their characterization. This is a crucial missing link for understanding the origin of planetary systems.

Dynamical interactions between a gaseous disc and a massive accreting planet produce structures such as gaps, spiral arms, and vortices (Goldreich & Tremaine 1980; Lin & Papaloizou 1986; de Val-Borro et al. 2007). Correlations between these structures and the presence of embedded planets have been studied in dust continuum and scattered light observations (e.g. Dipierro et al. 2015; Dong et al. 2015; Bae & Zhu 2018), potentially constraining the location and mass of the putative planets. However, several other mechanisms account for these observations, as exemplified by the diversity of theories that explain the HL Tau ring system (Lorén-Aguilar & Bate 2015; Okuzumi et al. 2016; Dullemond & Penzlin 2018).

Density perturbations induced by massive planets also bear kinematic counterparts. In the presence of a planet embedded in the disc, two spiral wakes develop in co-rotation with the perturber. In addition, the gas performs horseshoe orbits where, for a giant planet, a U-turn is present near the CPD (e.g. Machida et al. 2008). If the viscosity is low enough, a vortex is also prone to develop at the edge of the gap (e.g. Li et al. 2001), which consists in a subtle modulation on top of the gas Keplerian motion (Dullemond 2013). Do these distinct kinematic features bear an observable footprint in the Doppler maps of molecular lines? Are these signatures within the reach of current instrumentation, and can they lift the degeneracies in estimates based on the density field only?

Few works have studied the observability of planet-induced structures in molecular lines (Cleeves, Bergin & Harries 2015; Facchini et al. 2018), and fewer address their impact on the kinematics. For example, Ober et al. (2015) studied planet-carved gaps in line maps while assuming Keplerian velocities.

In a previous work we examined the vicinity of the CPD in channel maps (Perez et al. 2015), i.e. we considered the observability of CPDs by characterizing their morphology and kinematics in CO datacubes using radiative transfer applied to

★ E-mail: sebastian.astrophysics@gmail.com (SP); simon@das.uchile.cl (SC)

Smooth Particle Hydrodynamic (SPH) simulations, and subsequent filtering for the *uv*-coverage of the visibility plane of the Atacama Large Millimetre/submillimetre Array (ALMA) Observatory. We found three distinct CPD signposts at the vicinity of the protoplanet: (1) compact emission separated in velocity from the overall Keplerian disc, (2) a pronounced kink on the Doppler-shifted line emission as it sweeps across the CPD, and (3) a local increase in the dispersion at the protoplanet position. The latter allows us to measure the size of the CPD, which can be used as a proxy for the mass of the protoplanet (Perez et al. 2015) – the radius of a CPD is one-third to one-half of the planet's Hill sphere radius (e.g. Gressel et al. 2013). These signposts are detectable at the spatial and spectral resolutions available in CO(2-1) in the extended ALMA array configurations.

Here, we address whether planet–disc interactions can alter the velocity field to a level that makes the induced perturbations detectable. To this end, we perform 3D hydrodynamic simulations of gap-opening planets embedded in locally isothermal discs (Section 2). These new simulations follow the evolution of the disc over a longer time-scale and with a larger radial domain than our 2015 calculations, allowing us to study large-scale structures (Section 2.1). We combine these simulations with 3D Monte Carlo radiative transfer to calculate synthetic velocity maps (first moments) of the ^{12}CO line (Section 2.2). The outcome of the simulations and the predictions are then probed for kinematic signposts inherent to planet–disc interactions (Section 3). Implications are summarized in Section 4.

2 METHODS

2.1 3D hydrodynamic simulations

The hydrodynamical evolution of a gaseous disc with an embedded giant planet is simulated using the FARGO3D code (Version 1.2, Benítez-Llambay & Masset 2016), with the FARGO algorithm activated (Masset 2000). Fluid equations are solved in a spherical grid, where radius, azimuth, and colatitude are denoted by r, ϕ, and θ, respectively.

The equation of state is chosen as locally isothermal. This simplifying assumption, although far from being a realistic approximation, is enough to produce the planet–disc interactions' structures we aim to study in the kinematics, and even form a CPD around the planet (Gressel et al. 2013).

A planet is fixed on a circular orbit of radius r_p. The grid domain spans from 0 to 2π in ϕ, $0.4r_\mathrm{p}$ to $4r_\mathrm{p}$ in r, and $\pi/2 - 0.3$ to $\pi/2$ (the disc mid-plane) in θ, covering at least three vertical scale heights ($H = h/r$) within the domain. The mesh is evenly spaced in all directions using $(n_r, n_\phi, n_\theta) = (400 \times 600 \times 40)$ grid cells. The planet's potential is softened over a scale $0.3H$, which is of the order of the size of a CPD around a Jupiter-like planet at 100 au. The mass of the planet is gradually increased over the first few orbits using a tapering function.

The density and azimuthal velocity fields are extrapolated at the radial boundaries (Benítez-Llambay & Masset 2016), with reflecting boundary conditions at the mid-plane. Damping buffer zones near the radial boundaries of the mesh minimize spurious reflections (de Val-Borro et al. 2006). The units of the calculations are such that the gravitational constant, the stellar mass, and the size of the planet's orbit, r_p, are all equal to one.

We adopt an α-viscous model for the disk, and set $\alpha = 10^{-4}$. This α value allows vortices produced at the gap edge to be sustained for thousands of orbits (Fu et al. 2014). The aspect ratio of the disc is set to $h = h_0(r/r_\mathrm{p})^f$, with $h_0 = 0.08$ and $f = 0.15$. The initial surface density is $\Sigma = \Sigma_0(r/r_\mathrm{p})^{-1}$, with $\Sigma_0 = 0.09$ g cm^{-2} at $r_\mathrm{p} = 100$ au (total disc mass is 7×10^{-4} $M_\odot$). We adopt a 1 $M_\odot$ star. As the disc is not self-gravitating and does not exerts back-reaction onto the planet, the value of Σ_0 does not have any impact on the dynamics of the system. However, we note that it does have an effect on the optical depth of the emission line. This is addressed towards the end of Section 3.

The initial condition corresponds to the steady-state solution assuming hydrostatic equilibrium in the vertical direction (see Masset & Benítez-Llambay 2016, Appendix A). We then carry out three different simulations, each starts from the same initial condition, including a giant planet of 1, 5, or 10 Jupiter masses, labelled `P01J`, `P05J` and `P10J`, respectively. Further disc properties are presented in physical units in Section 2.2. Throughout the paper, whenever time is given in 'orbits', it refers to the orbital period at the planet's location, i.e. about 1000 yr for r_p=100 au.

These simulations were performed using the parallel Graphics Processing Unit (GPU) mode of FARGO3D. GPU acceleration allows full 3D hydrodynamic simulations of large discs to be evolved over long time-scales. A GPU cluster with four Tesla K80 HPC cards with enabled Peer-to-Peer communications between GPUs (Benítez-Llambay & Masset 2016), reached an average performance of $\sim$20 orbits h^{-1} for the simulations described here.

2.2 3D radiative transfer

Our choice of observables are spectrally and spatially resolved moment maps which are calculated from synthetic CO channel maps. Centred at 230.538 GHz, the ^{12}CO $J = 2$–1 emission line is bright and routinely observed by millimetre interferometers (it falls within ALMA's Band-6). We compute these synthetic images using the radiative transfer code FARGO3D-3D (version 0.41, Dullemond et al. 2012). We note that these predictions are valid for similar transitions (e.g. ^{12}CO $J = 3$–2 or $J = 6$–5) in LTE. The density and velocity fields obtained from the hydrodynamical simulations are first scaled to $r_\mathrm{p} = 100$ au and then input in RADMC-3D, preserving their grid structure and resolution.

A 7000 K star with 1 $R_\odot$ is placed at the centre of the grid. In addition, a mock dust distribution consisting of a mix of 30 per cent carbon and 70 per cent silicates is added following the simulated gas density. This dust distribution is only used to perform the temperature calculation via the Monte Carlo RADMC-3D module `mctherm`. Studying the continuum emission arising from dust thermal radiation requires a proper treatment of dust coupling through multifluid simulations (Baruteau & Zhu 2016) and is beyond the scope of this paper. We caution that our predictions do not take into account optical depth effects due to dust opacities.

Line radiative transfer is done in non-LTE with the Large Velocity Gradient (Sobolev) mode in RADMC-3D. The molecular data is from the LAMDA data base. Line widths include thermal broadening and a local (spatially unresolved) microscopic turbulence set to a constant value of 0.1 km s^{-1}. The ^{12}CO abundance relative to molecular hydrogen is assumed to be the standard value 10^{-4}. Our nominal simulated discs are inclined by 20° around a PA of 140° (east of north). The disc near side is the south-west and its rotation is counter-clockwise.

The resulting synthetic cubes have a total bandwidth of 6 km s^{-1}, with 120 individual channels of 0.05 km s^{-1} each. These synthetic data cubes represent our sky model which is subsequently convolved with a 50 mas circular beam (a standard angular resolution in ALMA

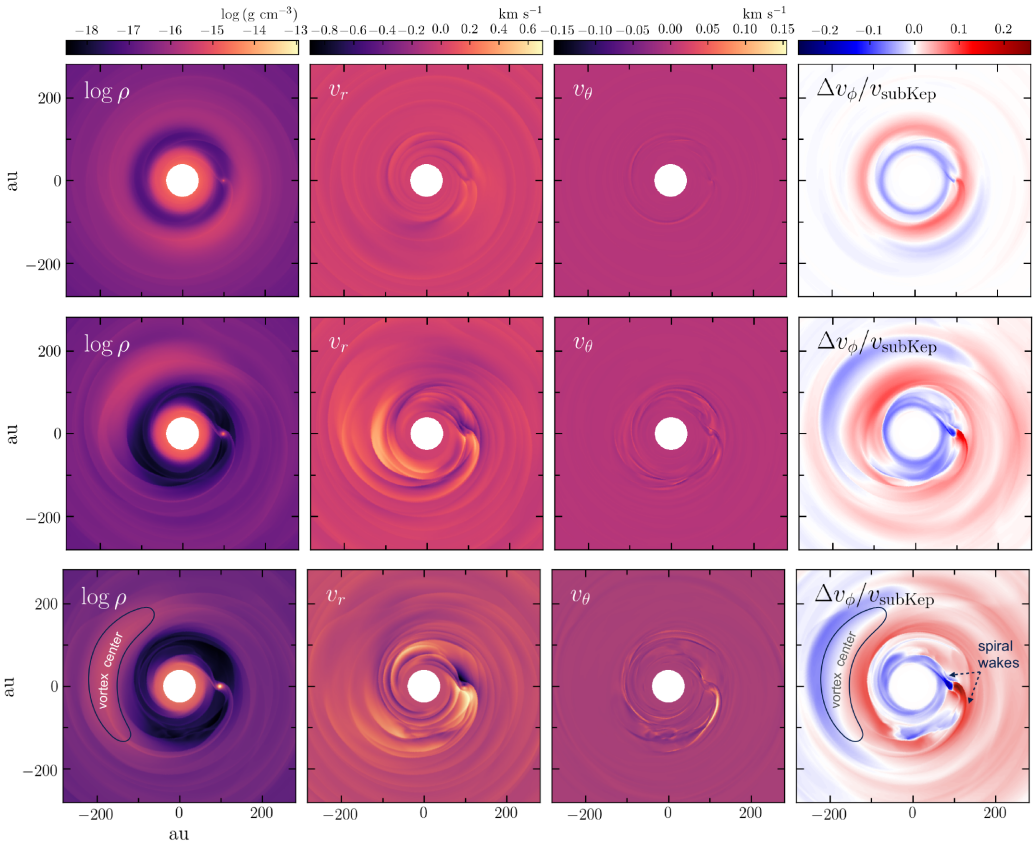

Figure 1. Simulation results for `P01J` (1 $M_{\rm Jup}$, top row), `P05J` (5 $M_{\rm Jup}$, middle), and `P10J` (10 $M_{\rm Jup}$, bottom) in the mid-plane after 1000 orbits. Left to right: Logarithm of the gas density (ρ), radial velocity ($v_{\rm r}$), colatitude velocity (v_θ), and the deviations from the sub-Keplerian equilibrium solution in the azimuthal component $\Delta v_\phi / v_{\rm subKep}$. Values are in physical units. Simulations are scaled to $r_{\rm p} = 100$ au. The gaps, spiral wakes, and vortices are prominent in all three simulations. In v_θ, positive values represent gas moving towards the mid-plane, while $v_{\rm r} > 0$ represents gas moving outwards. The disc rotation is counter-clockwise. The vortex and spiral wakes are labelled in the bottom right panel.

Band 6 observations). Our observables correspond to the intensity-weighted velocity centroid of the Doppler-shifted line emission (first moment maps). Since no dust is considered at the ray-tracing stage, the synthetic line emission cubes do not suffer from continuum over subtraction due to CO absorption (see Boehler et al. 2017, their fig. 8).

To address the observability of the planet–disc interaction signatures under realistic observing conditions, we first scale our ^{12}CO emission maps to an average flux density of 30 mJy beam^{-1} (in a 50 mas beam) at 100 au (similar to the flux levels reported for TW Hya, Huang et al. 2018), then we input these into CASA 5.1 `simobserve`. A 10 h integration in configuration C43-9 (13.8 km baseline) combined with a 3 h integration in C43-5 (1.4 km baseline) is needed to produce a well-sampled *uv*-coverage that unambiguously recovers the signatures (calibrations will require a similar amount of time). We further corrupted the visibilities with the task `ms.corrupt()` to obtain an RMS level in each 0.25 km s^{-1} channel of ∼1 mJy beam^{-1}. The beam is ∼50 × 80 mas beam (Briggs weighting 0.5). The signal-to-noise achieved at the planet's radius is ∼30. The low inclination of our synthetic disc (i=20°) implies that a high spectral resolution (0.25 km s^{-1}) is required to resolve the kinematics. The exact observing times and configurations required will depend on specific properties of the target. For example, for higher inclination angles the kinematics can be traced with lower spectral resolution. Finally, the first moment maps were computed in the CLEANed spectral cubes (produced with CASA `tclean`) by performing a Gaussian fit. The centroids of these Gaussians comprise the velocity fields shown in the fourth column in Fig. 3.

The temperature field obtained via the Monte Carlo solution of thermal equilibrium yields similar values to the isothermal power law used in the hydro simulation. The temperatures in our RT domain within 200 au are well above 25 K, preventing CO freeze-out from being an issue. The sound speed at the location of the planet is of the order of ∼90 m s^{-1}, which is small compared to the deviations in Keplerian motion which we present in Section 3. Heating from the planet is not considered in our calculation – its impact would be at small scales near the CPD. Changes in the thermodynamics of the whole disc, e.g. an adiabatic disc where compressional heating from spiral wakes becomes relevant, could in principle produce distinct kinematic signatures. Exploring these thermodynamic effects is beyond the scope of our paper.

3 RESULTS

Mid-plane densities after 1000 orbits are shown in the left column of Fig. 1. The gap edge is Rossby unstable, leading to the formation of a large-scale vortex in the outer disc (Lovelace et al. 1999; Varnière & Tagger 2006). The vortex is stable and long-lived due to our choice of low viscosity (Fu et al. 2014). After 1000 orbits, well-defined gaps, spiral wakes in the inner and outer disc, as well as a lopsided overdensity region in the outer disc are observed in all our simulations. Detailed descriptions of these structures as density

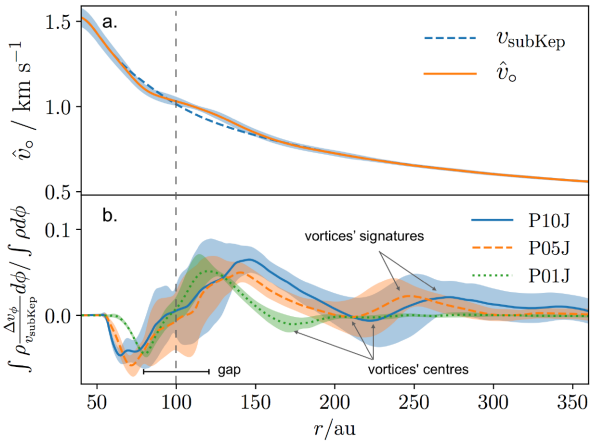

Figure 2. (a) Average 'observed' (projected onto the line-of-sight) Keplerian profile $\hat{v}_\circ$ calculated from the synthetic moment $v_\circ$ in Fig. 3. (b) Density-weighted average along the azimuthal axis for $\Delta v_\phi / v_{\rm subKep}$ (see Fig. 1), as a function of radius. The profiles' standard deviations are shown as a shaded area around the average values.

features are found elsewhere in the literature (e.g. Fu et al. 2014; Bae & Zhu 2018; Hammer, Kratter & Lin 2017).

In the absence of a perturber, the disc follows a nearly pure Keplerian motion $v_{\rm subKep}$, with $v_{\rm r}$ and v_θ values that are negligible compared to the local azimuthal velocity. An observation of such unperturbed disc, inclined w.r.t the line-of-sight, displays a velocity field whose isovelocity contours follow a characteristic 'dipole pattern'. This Keplerian pattern is symmetric w.r.t a straight line at systemic velocity, parallel to the disc's minor axis.

Figs 1 and 2 allow us to study the kinematics of gaps, spiral wakes, and vortices, while Fig. 3 shows the observable counterparts of these structures. Fig. 1 shows the evolved velocity fields $v_{\rm r}$ and v_θ (middle panels), and the relative deviations from Keplerian rotation $(v_\phi - v_{\rm subKep})/v_{\rm subKep}$ (right panels) after 1000 orbits. Radial profiles of the azimuthal deviations are shown in Fig. 2. In turn, Fig. 3 shows isovelocity contours in the predicted ^{12}CO(2-1) line centroids $v_\circ$. The largest deviations occur close to the planet, near the CPD. The observability of this CPD signature requires observations with a resolution comparable to the size of the CPD (∼1/3 Hill radius) and is described in Perez et al. (2015).

Relative deviations $\Delta v_\phi / v_{\rm subKep}$ from Keplerian motion are notorious in the gap for all simulations. As the gas in the outer wall speeds up, the inner wall slows down producing zones where gas transitions from below sub-Keplerian to *super* Keplerian. For large planet masses (`P05J` and `P10J`), $v_{\rm r}$ and v_θ values can grow up to ∼20 per cent of the local azimuthal speed, while for 1 $M_{\rm Jup}$ these values increase only up to 1–5 per cent the local azimuthal speed (∼3 km s^{-1} at 100 au). These perturbations are induced by gravitational forces exerted by the planet as well as pressure and viscous forces. In our isothermal simulations, the pressure field is proportional to the density field (left panels in Fig. 1) multiplied by $1/r$.

Across the gap (between ∼80 and ∼120 au), there is a gradient in the azimuthal average of $\Delta v_\phi / v_{\rm subKep}$. Here the mean deviation increases monotonically from -5 to +5 per cent (Fig. 2b). This is shared by all our simulations. At 100 au, this gradient translates into a ∼0.3 km s^{-1}deviation which is indeed observable, but its magnitude does not depend strongly on the planet's mass.

The maximum departure from Keplerianity occurs at the outer spiral wake, where a strong dependency with the mass of the planet is observed, with maximum deviations of 26, 18, and 9 per cent for `P10J`, `P05J`, and `P01J`, respectively. This is demonstrated in Fig. 2(a). v_θ traces the departure from hydrostatic equilibrium which, as expected, is stronger at the spiral wake where material streams in from the poles onto the CPD.

The vortex signature appears in $\Delta v_\phi / v_{\rm subKep}$ as a subtle motion on top of the Keplerian disc. The side of the vortex which is closest to the gap is faster than $v_{\rm subKep}$, while the outer part is slower. The strength of this super-Keplerian region depends on the perturber's mass. Fig. 2(b) shows that at radii larger than the vortex centre the peak Keplerian deviations attain up to 5 per cent for `P05J` and `P10J`, but negligible (< 1 per cent) for `P01J`. The bottom panel displays that these deviations are significant in the azimuthal average as well, with up to 2-3 per cent deviation over the outer disc.

The first moment prediction for our three simulations are shown in Fig. 3. The isovelocity contours in the line centroids $v_\circ$ show wiggling substructure over various areas in the disc, becoming ubiquitous and strong for `P05J` and `P10J`. These wiggling structures correspond to parcels of gas that experience pressure gradients that make them attain values from below sub-Keplerian to super-Keplerian motion (see $\Delta v_\phi / v_{\rm subKep}$ maps in Fig. 1). These pressure gradients are mainly due to gravitational interactions with the embedded planet. The gas within the gap experiences such pressure gradients, leading to a sawtooth signature in the isovelocity contours at all azimuths.

In first approximation the wiggles in the sky map $v_\circ(\vec{x})$ are perturbations on an approximately Keplerian background flow, $\hat{v}_\circ(\vec{x})$. This background flow includes modulations from the line optical depth $\tau(\vec{x})$, especially at the outer gap edge. We use $v_\circ(\vec{x})$ directly to estimate $\hat{v}_\circ(\vec{x})$, as would be done for an actual observation. We deproject $v_\circ(\vec{x})$ by the disk inclination (e.g. as in Casassus et al. 2018), transform to polar coordinates about the star, and fit $v_\circ(r, \phi)$ with a harmonic modulation of the form $\hat{v}_\circ(r, \phi) = \hat{v}(r)\cos(\phi)$. A projection back to the sky plane gives $\hat{v}_\circ(\vec{x})$. The profile $\hat{v}_\circ$ is shown in Fig. 2a, where it is compared against a prediction $v_{\rm subKep}(r)$ calculated in the same way as $\hat{v}_\circ$ but from a prediction where the gas is forced to follow pure sub-Keplerian motion. We see that $|(v_{\rm subKep}(r) - \hat{v}(r))| \lesssim \hat{\sigma}(r)$, where $\hat{\sigma}(r)$ is the standard deviation of the perturbations $\sqrt{\langle (v_\circ - \hat{v})^2 \rangle_\phi}$ along azimuth, confirming that $\hat{v}(r)$ is a good proxy for the unperturbed flow. We see from Fig. 3 that the sharp rise in $\tau(\vec{x})$ at the outer gap edge results in a shallow wiggle of $v_\circ(\vec{x})$, much smaller than the perturbations over $\hat{v}(\vec{x})$. We note that, for discs with larger inclinations and significant flaring, a conical transformation would work better than the simple polar mapping we apply here.

The difference between $\hat{v}_\circ(\vec{x})$ and $v_\circ(\vec{x})$ allows us to remove optical depth effects and quantify the strength of the dynamical influence of a planet (lower panels in Fig. 3). Deviations solely due to planet–disc interactions range from −0.15 to +0.15 km s^{-1} over spatial scales comparable to the gap width and the azimuthal expanse of the trailing wake and vortex.

We identify the strongest wiggles near the outer spiral wake and in front of the CPD (our mock disc rotates counter-clockwise). This is quantified in the bottom panels of Fig. 3, which show the magnitude of these deviations after the subtraction of a Keplerian first moment map. The maximal deviation is seen when the planet is near the disc's minor axis. This signature decreases when the planet approaches the disc PA (see animation in Fig. 3). Upon crossing the disc minor axis, the sign of the deviation changes. When a parcel of super Keplerian gas is on the redshifted (blueshifted) half of the disc, it will be redder (bluer) than Keplerian, pulling the isovelocity contours ahead. Gas moving below Keplerian speed has a signature in the opposite direction. The outer spiral wake corresponds to gas

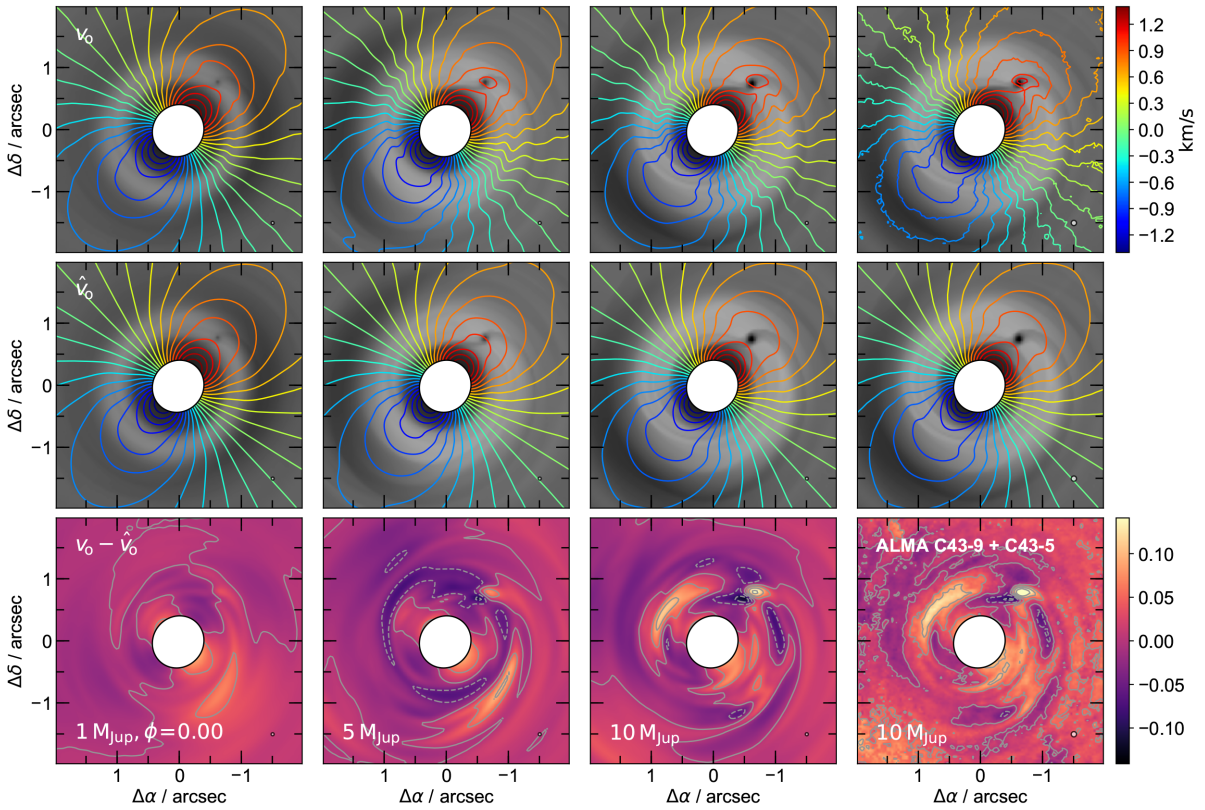

Figure 3. Upper panels show the first moment map ($v_\circ$) predictions in ^{12}CO(2-1) with embedded companions of (from left to right) 1, 5, and 10 M$_{\rm Jup}$, after 1000 orbits (∼0.5 Myr) and convolved with a 50 mas beam. The fourth column (right) shows the prediction for the 10 M$_{\rm Jup}$ case after filtering through ALMA Cycle 6's uv-coverage (configuration C43-9 plus C43-5) with an RMS noise of ∼1 mJy beam^{-1} (see Section 2.2). Click to play a short movie showing how the first moments change with the location of the planet (ADOBE READER recommended). The first frame shows the planet along the disc PA. The underlying grey-color maps show the dust continuum following the same density as the gas. These continuum maps are only used to highlight the positions of the companions and vortices. Middle panels show $\hat{v}_\circ$ computed directly from the $v_\circ$ (see Section 3), which serve as a proxy for the unperturbed Keplerian disc profile. Contours show the projected velocities with colours ranging from -1.4 (blue) to 1.4 km s^{-1} (red), in steps of 0.15 km s^{-1}. The bottom panels show the deviation from Keplerianity, i.e. the difference between top and middle panels. The x- and y-axes show angular offset from the stellar position in arcsecond.

at super Keplerian speed and its signature appears as a sawtooth or kink in $v_\circ$. `P05J` and `P10J` develop secondary and tertiary spiral arms in the inner disc which also bear a kink in the isovelocity contours.

4 SUMMARY

We performed 3D hydrodynamic simulations to study the dynamical impact of a planet in the velocity field of circumstellar gas. Kinematical counterparts in the three components of the velocity field were identified for the planet's spiral wakes, the gap, and the outer disc vortex. The observability of these kinematic structures was then studied by computing first moment maps of ^{12}CO line emission using 3D radiative transfer.

Discs with embedded planets produce deviations from Keplerian kinematics which are observable at ALMA resolutions. The magnitude of these deviations depend on the mass of the planet and they are most notorious at the locations of the spiral wakes, across the gap, and at the inner secondary (and tertiary) arms.

We conclude that evidence for planet–disc interaction can be detected by probing for non Keplerian motion in the velocity field of nearby discs. In principle the measurement of the corresponding protoplanet masses can be achieved by comparison with hydrodynamical simulations, further work is needed to assess model biases with the inclusion of radiation transport, planet heating, and the impact of multiple and/or eccentric planets. From this initial study, we anticipate that 50 mas resolutions are sufficient to pick up the kinematic signal of a ≥1 M$_{\rm Jup}$ planet at 1 arcsec (100 au) around a 1 M$_\odot$ star.

During the review process of this letter two new articles reported the kinematic detection of protoplanets in molecular line observations of HD 163296. Pinte et al. (2018) observed the kink in the isovelocity maps due to an embedded planet, as in the generic predictions by Perez et al. (2015), thus identifying the presence of a giant planet at 260 au. The planet-to-star mass ratio puts this detection in a similar regime as our new 1 M$_{\rm Jup}$ simulation, but the line data set used by Pinte et al. (2018) is not deep enough to produce a first moment map with which to test for the large-scale signatures that we report here. While their simulations indeed reproduce the localized signature (i.e. the kink), the large-scale kinematic structures are not present, which may be due to the short time span of their SPH calculation. At the same time, Teague et al. (2018) detected the radial modulation in the averaged azimuthal velocity imparted by the pressure gradient in two gaps, at 83 and 137 au, which can be explained by embedded protoplanets.

In this new letter, we have improved our 2015 predictions with simulations over long time spans which have reached steady state, thanks to which we find that the kinematic perturbations from planet–disc interactions extend over large scales in the disk. We

propose that this large-scale structure can be used to distinguish the origin of the velocity perturbations, and eventually pinpoint the perturbers where the deviations from Keplerian rotation changes sign.

ACKNOWLEDGEMENTS

We thank the anonymous reviewer for helpful comments. We acknowledge support from the government of Chile grants Millennium Scientific Initiative RC130007, CONICYT-Gemini 32130007, and FONDECYT 1171624. S.P thanks Anya Yermakova for useful comments and discussions. These simulations were run with the Brelka cluster, hosted at DAS/U. de Chile (Fondequip EQM140101). This project has received funding from the European Union's Horizon 2020 research and innovation programme under grant agreement no. 748544 (PB-L).

REFERENCES

Bae J., Zhu Z., 2018, ApJ, 859, 119
Baruteau C., Zhu Z., 2016, MNRAS, 458, 3927
Benítez-Llambay P., Masset F. S., 2016, ApJS, 223, 11
Boehler Y., Weaver E., Isella A., Ricci L., Grady C., Carpenter J., Perez L., 2017, ApJ, 840, 60
Casassus S. et al., 2018, MNRAS, 477, 5104,
Cleeves L. I., Bergin E. A., Harries T. J., 2015, ApJ, 807, 2
de Val-Borro M. et al., 2006, MNRAS, 370, 529
de Val-Borro M., Artymowicz P., D'Angelo G., Peplinski A., 2007, A&A, 471, 1043
Dipierro G., Price D., Laibe G., Hirsh K., Cerioli A., Lodato G., 2015, MNRAS, 453, L73
Dong R., Zhu Z., Rafikov R. R., Stone J. M., 2015, ApJ, 809, L5
Dullemond C., 2013, EPJ Web of Conferences, 46, 01001
Dullemond C. P., Penzlin A. B. T., 2018, A&A, 609, A50
Dullemond C. P., Juhasz. A., Pohl A., Sereshti F., Shetty R., Peters T., Commercon B., Flock M., 2012, Astrophysics Source Code Library, record ascl:1202.015
Facchini S., Pinilla P., van Dishoeck E. F., de Juan Ovelar M., A&A, 2018, 612, A104
Follette K. B., , et al., 2017, AJ, 153, 264
Fu W., Li H., Lubow S., Li S., 2014, ApJ, 788, L41
Goldreich P., Tremaine S., 1980, ApJ, 241, 425
Gressel O., Nelson R. P., Turner N. J., Ziegler U., 2013, ApJ, 779, 59
Hammer M., Kratter K. M., Lin M.-K., 2017, MNRAS, 466, 3533
Hord B., Lyra W., Flock M., Turner N. J., Mac Low M.-M., 2017, ApJ, 849, 164
Huang J., , et al., 2018, ApJ, 852, 122
Li H., Colgate S. A., Wendroff B., Liska R., 2001, ApJ, 551, 874
Lin D. N. C., Papaloizou J., 1986, ApJ, 307, 395
Lorén-Aguilar P., Bate M. R., 2015, MNRAS, 453, L78
Lovelace R. V. E., Li H., Colgate S. A., Nelson A. F., 1999, ApJ, 513, 805
Machida M. N., Kokubo E, Inutsuka S., Matsumoto T., 2008, ApJ, 685, 1220
Masset F., 2000, A&AS, 141, 165
Masset F. S., Benítez-Llambay P., 2016, ApJ, 817, 19
Ober F., Wolf S., Uribe A. L., Klahr H. H., 2015, A&A, 579, A105
Okuzumi S., Momose M., Sirono S., Kobayashi H., Tanaka H., 2016, ApJ, 821, 82
Perez S., Dunhill A.., Casassus S., Roman P., Szulágyi J., flores C., Marino S., Montesinos M., 2015b, ApJ, 811, L5
Pinte C. et al., 2018, ApJ, 860, L13
Sallum S. et al., 2015, Natur, 527, 342
Spiegel D. S., Burrows A., 2012, ApJ, 745, 174
Teague R., Bae J., Bergin E., Birnstiel T., Foreman-Mackey D., 2018, ApJ, 860, L12
Thalmann C. et al., 2016, ApJ, 828, L17
Varnière P., Tagger M., 2006, A&A, 446, L13

SUPPORTING INFORMATION

Supplementary data are available at *MNRASL* online.

movie_m1_avg_simobserve_12co21_Rs100.mov
movie_m1_avg_simobserve_12co21_Rs100_hires.mov

Please note: Oxford University Press is not responsible for the content or functionality of any supporting materials supplied by the authors. Any queries (other than missing material) should be directed to the corresponding author for the article.

This paper has been typeset from a TEX/LATEX file prepared by the author.